Acta Materialia 144 (2018) 80–91

Contents lists available at ScienceDirect

Acta Materialia

journal homepage: www.elsevier.com/locate/actamat

Full length article

Microstructure and mechanical properties of a precipitation-strengthened Al-Zr-Sc-Er-Si alloy with a very small Sc content

Anthony De Luca [a, *], David C. Dunand [a, b], David N. Seidman [a, b, c]

[a] Northwestern University, Department of Materials Science and Engineering, 2220 Campus Drive, Evanston, IL 60208-3108 USA
[b] NanoAl LLC, Illinois Science + Technology Park, 8025 Lamon Ave, Suite 446, Skokie, IL 60077 USA
[c] Northwestern University Center for Atom-Probe Tomography, 2220 Campus Drive, Evanston, IL 60208-3108 USA

ARTICLE INFO

Article history:
Received 21 August 2017
Received in revised form
16 October 2017
Accepted 16 October 2017
Available online 5 November 2017

Keywords:
Al-Zr-Sc-Er-Si alloy
Atom-probe tomography
Precipitation strengthening
High-temperature alloy
Mechanical properties

ABSTRACT

The precipitation hardening behavior of an Al-0.08Zr-0.014Sc-0.008Er-0.10Si (at.%) alloy was investigated utilizing microhardness, electrical conductivity, atom-probe tomography (APT), and compressive creep-measurements. This new composition, with a Sc:Zr atomic ratio of less than 1:5 represents a significant reduction of the alloy's cost when compared to the more usual Al-0.06Sc-0.02Zr based alloys with typical Sc:Zr atomic ratios of 3:1. To study the precipitation behavior of this *low-Sc alloy*, isothermal aging experiments between 350 and 425 °C for a duration of up to 6 months were performed. The low concentration of Sc, compensated by the high Zr concentration, permits the alloy to achieve a higher peak microhardness than the corresponding Sc-richer, Zr-leaner alloys. The *low-Sc alloy* also shows better over aging resistance, as anticipated from the smaller diffusivity of Zr when compared to Sc, leading to slower coarsening kinetics. Atom-probe tomography demonstrates that the high microhardness is due to the formation of a high number density of nano-precipitates, ~10^{23} m^{-3} for peak aging conditions, with a mean radius of 1.9 nm, thus yielding a high volume fraction (0.35%) of nano-precipitates. Like alloys with much higher Sc and Er concentrations, the $(Al,Si)_3(Sc,Zr,Er)$ nano-precipitates still exhibit a core-shell structure with a concentration of Zr in the shell of up to 25 at.%, and a Sc- and Er-enriched core. Compressive creep experiments at 300 °C demonstrate that the new alloy, with only 0.014 at% Sc, is as creep resistant as a binary Al-0.08Sc at.% alloy, displaying a threshold stress of 17.5 ± 0.6 MPa at peak aged condition.

© 2017 Acta Materialia Inc. Published by Elsevier Ltd. All rights reserved.

1. Introduction

The automotive industry has steadily reduced the environmental footprint of vehicles by making more efficient use of fuel. One way to achieve this goal is to decrease vehicle mass by an increased use of low-density aluminum alloys. Most commercial aluminum alloys are, however, limited to low temperatures (i.e., below ~225 to 250 °C) due to the dissolution or phase transformation of their strengthening precipitates. To deploy aluminum alloys for high temperature applications in automotive and aerospace, one approach is to create coherent $L1_2$ precipitates containing slow-diffusing elements, which strengthen the alloy by impeding dislocation motion and are stable and coarsen only slowly by diffusion at the operating temperature [1].

During the last decade, dozens of $L1_2$ forming Al-alloys have been investigated, with micro-additions of one to five elements [2–30]. These Al-alloys are aimed at optimizing the strength of Al-alloys by achieving higher processing temperatures and maintaining reasonable prices. Building on an alloy studied by Vo et al. [26,29],we engineered a *low-Sc*, high-Zr Al-Zr-Sc-Er-Si alloy [30]. Addition of Zr to Al-Sc alloys improves the coarsening resistance of the $L1_2$ precipitates by forming a Zr-enriched shell around a Sc-enriched core, to form a core/shell precipitates. Al_3Zr however has a smaller lattice parameter mismatch with the Al matrix than Al_3Sc [16]. Replacement of Sc by Zr in this shell reduces the creep strength of the alloy. By contrast, adding Er accelerates the nucleation rate of the $L1_2$ precipitates, forms an Er-enriched core, and since Al_3Er has a larger lattice parameter mismatch with the matrix than does Al_3Sc it markedly improves the creep strength [7,8]. Addition of Er to Al-Sc-Zr alloys thus compensates for the smaller lattice parameter mismatch of the Zr-enriched core [17]. Alternatively, silicon accelerates diffusion and precipitation kinetics of the

* Corresponding author.
E-mail address: anthony.deluca@northwestern.edu (A. De Luca).

https://doi.org/10.1016/j.actamat.2017.10.040
1359-6454/© 2017 Acta Materialia Inc. Published by Elsevier Ltd. All rights reserved.

$L1_2$ formers [20,26,29]. The effect of Si on the $L1_2$ precipitate-matrix lattice parameter mismatch is, however, unknown. The newly investigated Al-0.08Zr-0.014Sc-0.008Er-0.10Si at.% alloy [30], represents a drastic reduction of price, because Sc is extremely expensive. Utilizing the current prices of Sc, Zr, Er and Al (2017) of 15,000, 100, 95 and 0.44 USD/kg, respectively [31,32], the cost of the new alloy is ~6 USD/kg, compared to ~16 USD/kg for the previous Sc-richer composition; this is nearly a threefold decrease in cost. We previously demonstrated that the alloy achieved a similar peak microhardness of 587 ± 20 MPa as the Sc-richer alloy during isochronal aging [30]. The position of the peak shifted 50 °C toward higher temperatures yielding a better coarsening resistance than anticipated. An optimal single-step aging temperature was estimated to lie between 350 and 425 °C.

This article investigates the precipitation hardening behavior of the above *low-Sc alloy* during isothermal aging in the temperature range 350–425 °C. The alloy exhibits increased strength and coarsening resistance at the investigated temperatures compared to Sc-rich alloys, and is as strong as an Al-0.08Sc alloy when crept at 300 °C. APT investigation reveals that the higher strength achieved is due to the presence of a high number density and a high volume fraction of nanometer diameter precipitates.

2. Experimental procedures

An alloy with a nominal composition of Al-0.08Zr-0.02Sc-0.005Er-0.10Si at.% (Al-0.27Zr-0.03Sc-0.03Er-0.10Si wt.%), was melted in alumina crucibles in a resistively heated furnace by adding, to molten 99.99 at.% pure Al, appropriate amounts of Al-8.0 wt% Zr, Al-2 wt.% Sc, Al-3.9 wt% Er master alloys preheated to 640 °C and Al-12.6 wt% Si preheated at 450 °C. The melt was maintained in air for 1 h at 800 °C, regularly stirred, and then cast into a graphite mold. The mold was preheated to 200 °C and placed on an ice-cooled copper platen prior to casting to enhance directional solidification. The chemical composition of the as-cast alloy was measured by direct current plasma mass spectroscopy (DCPMS) at ATI Wah Chang (Albany, OR (Table 1). The iron concentration was less than the detection limit (<100 wt ppm). APT was also utilized to measure alloy chemical compositions, using the average values of ten specimens (cf. Table 1). The LEAP tomography results are in reasonable agreement with the DCPMS measurements. When compared, however, to the nominal composition, the Sc concentration is lower. In this article, we use the DCPMS composition of the alloy, Al-0.08Zr-0.014Sc-0.008Er-0.10Si at.%, and we express all compositions in atomic percent (at.%). For easier reading, and compared with other alloys, this alloy is denoted the *low Sc alloy*.

After quenching, the alloy was homogenized in air for 8 h at 640 °C, which was determined to be the optimized homogenization condition [30]. The alloy was then subjected to isothermal aging at 350, 375, 400 and 425 °C, for durations ranging from 20 min to 6 months. All heat treatments were performed in air and terminated by water quenching.

Vickers microhardness measurements were performed employing a Duramin-5 microhardness tester (Struers) utilizing an applied load of 200 g for 5 s on samples polished to at least a 1 μm surface finish. A minimum of ten and up to twenty indentations, on different grains, were made for each specimen. Electrical conductivity measurements were performed utilizing a Sigmatest 2.069 eddy current instrument (Foerster Instruments, Pittsburgh, PA). For each specimen, five measurements were made at 120, 240, 480, and 960 kHz.

Specimens for three-dimensional (3D) local-electrode atom-probe (LEAP) tomography were prepared by cutting with a diamond saw ~0.35 × 0.35 × 10 mm^3 blanks, which were electropolished at 20–25 VDC using a solution of 10% perchloric acid in acetic acid, followed by electropolishing at 12–18 VDC utilizing a solution of 2% perchloric acid in butoxyethanol, both at room temperature [33,34]. Pulsed-laser atom-probe tomography was performed utilizing a LEAP 4000X Si-X tomograph (Cameca Instruments Inc., Madison, WI) [35,36] at a specimen temperature of 30 K. Focused picosecond ultraviolet (UV) laser pulses (wavelength = 355 nm) with a laser beam waist of <5 μm at the e^{-2} diameter were utilized. Analyses were performed with a pulse frequency of 500 kHz while maintaining a detection rate of 1 or 2%. To reduce the white noise in the mass spectra for the Zr^{3+} ions due to the thermal tail of the Al^{1+} ions, the laser energy was adjusted for each experiment, and ranged between 15 and 24 pJ $pulse^{-1}$. This adjustment was achieved to obtain a compromise between a lower $Al^{1+/2+}$ ratio and low overall white noise in the mass spectra. LEAP tomographic data were analyzed employing IVAS v3.6.1 (Cameca Instruments). The LEAP datasets were reconstructed in the voltage mode and the initial nanotip radius was adjusted in to obtain the correct aluminum atomic interspacing for the observed crystallographic {hkl} planes.

Constant-load compressive creep experiments were performed at 300 °C, with a thermal fluctuation of ±1 °C. Cylindrical creep specimens with a 10 mm diameter and 20 mm height, were placed between boron-nitride-lubricated alumina platens, and heated in a three-zone furnace. Sample displacement was measured with a linear variable displacement transducer (LVDT) with a resolution of 10 μm. Minimum strain rates at a given stress were determined by measuring the slope of the strain vs. time line in the steady-state creep regime. The applied load was increased when a clear steady-state strain rate was observed. The total accumulated creep strain for each specimen was maintained below 10% to guarantee that the shape of the specimens remained cylindrical and the applied stress uniaxial.

Table 1
Composition (at.%) of the investigated alloy, as measured by direct plasma emission spectroscopy (DCPMS) and local-electrode atom-probe (LEAP) tomography.

	Zr	Sc	Er	Si
Nominal	0.08	0.02	0.0045	0.10
DCPMS	0.075	0.014	0.0075	0.094
LEAP	0.060	0.011	0.0025	0.094[a]

[a] Atomic concentration of $^{28}Si^{2+}$ ions in the LEAP tomographic mass spectrum.

3. Results

3.1. Isothermal aging at temperature ranging from 350 to 425 °C

The temporal evolution of the Vickers microhardness and electrical conductivities of the *low Sc alloy*, homogenized for 8 h at 640 °C, and then aged at 350, 375, 400 and 425 °C, are plotted as a function of aging time in Fig. 1. At 350 °C, the microhardness gradually increases from the as-homogenized state (251 ± 7 MPa) and peaks at 639 ± 29 MPa after aging for 40 h. This slow hardening rate is due to the sluggish diffusion of Zr at 350 °C. For longer aging times, the microhardness decreased slowly and stabilized at ~600 MPa between 3 weeks and 3 months. It later decreased to 554 ± 25 MPa after 6 months. The electrical conductivity (Fig. 1b) increased steadily from 30.06 ± 0.09 MS m^{-1} to 33.66 ± 0.07 MS m^{-1} after 40 h, indicating continuous precipitation. Beyond peak aging, the rate of change on the EC curve decreases with increasing aging times and after six months, the measured electrical conductivity was 34.94 ± 0.1 MS m^{-1}. The change in rate after 40 h indicates that the driving force for precipitation has been greatly reduced and the matrix composition is approaching equilibrium.

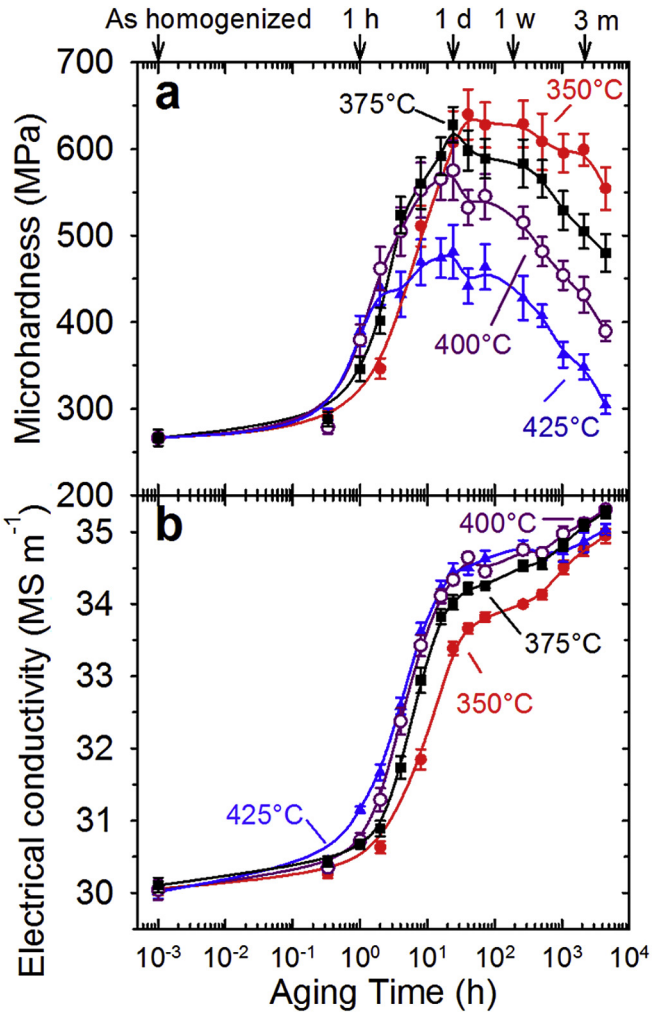

Fig. 1. Evolution of: a)Vickers microhardness; and b) electrical conductivity during isothermal aging at 350 °C (solid circles), 375 °C (squares), 400 °C (open circles) and 425 °C (triangles) of the *low Sc alloy* (Al-0.08Zr-0.014Sc-0.008Er-0.10Si at.%) homogenized at 640 °C for 8 h.

Since the isothermal aging experiments performed at 375, 400 and 425 °C exhibit similar trends, but different peak microhardness values, the microhardness and electrical conductivity curves are described together (Fig. 1). For the three temperatures, the peak microhardness was achieved after 24 h of aging, which is nearly half the required time for aging at 350 °C. The peak microhardness obtained for aging at 375, 400 and 425 °C are, respectively, 628 ± 20, 575 ± 34 and 481 ± 21 MPa. The microhardness then progressively decreased to 480 ± 22, 390 ± 12 and 304 ± 11 MPa after 6 months of aging. The electrical conductivity curves (Fig. 1b) follow the same trend at these higher temperatures as the curve at 350 °C, but are shifted toward shorter incubation times (onset of increase) with increasing temperature. For example, to achieve a conductivity of 31 MS m^{-1}, requires 160 min at 350 °C; for each increase of 25 °C, this time is reduced by ~40 min. Aside for the incubation time, the initial conductivity slopes are similar for the three temperatures and reaches the beginning of a plateau region after 24 h, corresponding to peak microhardness. The conductivities at the beginning of the plateaus are 34 ± 0.1 MS, 34.34 ± 0.06 and 34.45 ± 0.12 MS m^{-1}, respectively, at 375, 400 and 425 °C. For longer times, the conductivity continues to increase slowly, and achieves values after 6 months of 35.27 ± 0.08, 35.31 ± 0.05 MS and 35.03 ± 0.08 MS m^{-1}, respectively.

Based on the microhardness versus aging time curves (Fig. 1a), the best aging temperature is identified. At 375 °C the best combination of high peak microhardness (628 MPa) and short aging time (24 h) is achieved. Once peak-aged, the alloy is anticipated to maintain a stable microhardness for at least several months at 350 °C and lower.

The aging behavior at 400 and 425 °C of our *low Sc alloy* (Al-0.08Zr-0.014Sc-0.008Er-0.10Si) is compared in Fig. 2a and b to those of two previously investigated *high Sc, low Zr alloys*: Al-0.055Sc-0.005Er-0.02Zr-0.05Si (*high Sc alloy*, with low Si concentration) [26] and Al-0.055Sc-0.005Er-0.02Zr-0.12Si (high Sc alloy, with *high Si* concentration) [29]. Before aging, the *high Sc alloy* was homogenized at 640 °C for 72 h, while the *high Si alloy* was homogenized for 2 h. The *high Sc alloy* displays a fast hardening rate at 400 °C, needing only 12 min to achieve a microhardness of 493 ± 10 MPa. The microhardness then slowly increases with time, peaking at 533 ± 12 MPa after 60 h of aging. For longer aging times, the microhardness continuously decreases, reaching 412 ± 11 MPa after 3000 h (125 days). The *high Si alloy*, which contains the same concentration of Sc as the *high Sc alloy*, but more than twice the concentration of Si, displays a similarly fast increase of microhardness for a short aging time. It, however, achieves a peak

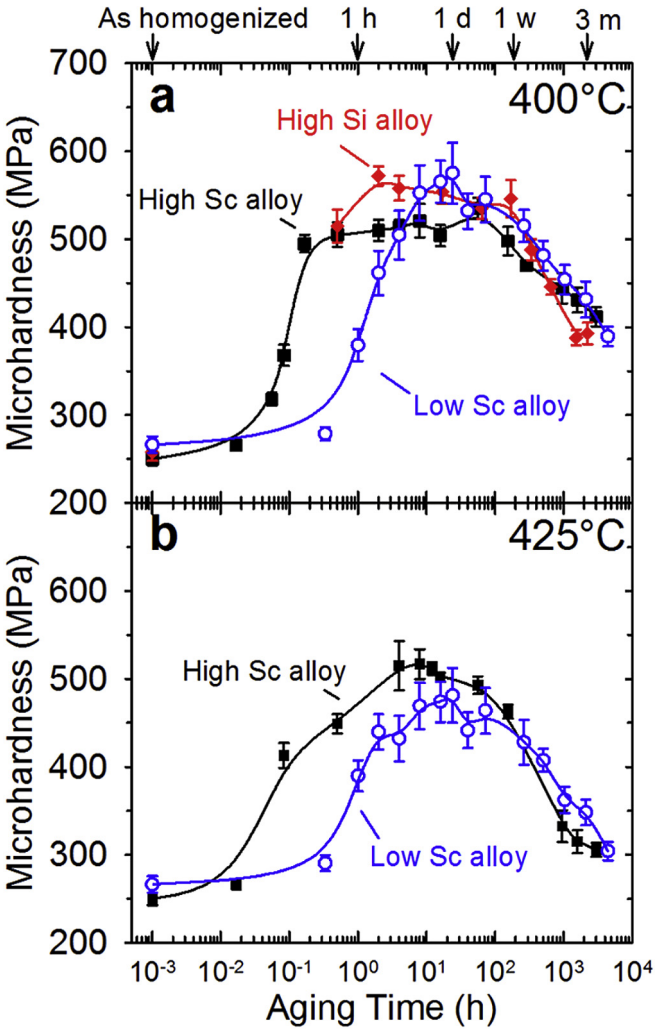

Fig. 2. Evolution of Vickers microhardness as function of aging time for aging temperature of: a) 400 °C; and b) 425 °C for three different Al-Sc-Er-Zr-Si alloys: Al-0.08Zr-0.014Sc-0.008Er-0.10Si at.% (*low Sc alloy*), Al-0.055Sc-0.005Er-0.02Zr-0.05Si at.% (*high Sc alloy*) [26] and Al-0.055Sc-0.005Er-0.02Zr-0.12Si at.% (*high Si alloy*) [29].

microhardness of 572 ± 11 MPa after 2 h of aging. The microhardness then slowly decreases during one week before displaying an abrupt loss of microhardness, decreasing to 400 MPa after 2 months. Increasing the Si concentration of silicon is beneficial for increasing the peak microhardness (7% higher), and achieving it much faster (2 h vs. 60 h), and the alloy maintained a microhardness >500 MPa for longer than one week. The faster decrease of the microhardness is an undesirable characteristic of this alloy [29]. At 425 °C (Fig. 2b), the *high Sc alloy*, needs 8 h to achieve a peak microhardness of 517 ± 17 MPa before commencing to decrease, with the microhardness decreasing to <400 MPa after ~360 h.

In our *low Sc alloy,* the critical substitution of the cheaper Zr for the expensive Sc has the strong effect of strongly decelerating the hardening process, taking twelve times longer than for the *high Si alloy* to reach a peak microhardness when aging at 400 °C (Fig. 2a). Nevertheless, the high peak microhardness was kept and reached 575 ± 34 MPa. After peak aging, the microhardness of the *low Sc alloy* follows a similar aging behavior as the *high Si alloy* for approximately two weeks. It, however, does not suffer the same later's rapid loss of microhardness, exhibiting a similar microhardness as the *high Sc alloy* for an aging duration >1000 h. At 425 °C, the *low Sc alloy* achieves a smaller peak microhardness than the *high Sc alloy* after longer aging times. It, however, displays a better over-aging resistance, as demonstrated by the slower decrease of microhardness (cf. Fig. 2b).

3.2. Nanoprecipitate characterization by atom-probe tomography

To identify the strengthening mechanism resulting from the nanoprecipitates, atom-probe tomography was performed on samples aged for 24 h at 375 or 400 °C (peak microhardness), aged 21 days at 375 °C or 11 days at 400 °C (overaged). The microstructures obtained for these four aging conditions are displayed in (Fig. 3). In those APT 3-D reconstructions the Sc, Er and Zr atoms are respectively indicated in red, blue and green. Aluminum and silicon atoms are omitted for clarity. The number density (N_v), mean radius ($\langle R \rangle$) and volume fraction (ϕ), measured for several analyzed volumes for each aging condition, reported in Table 2 and compared

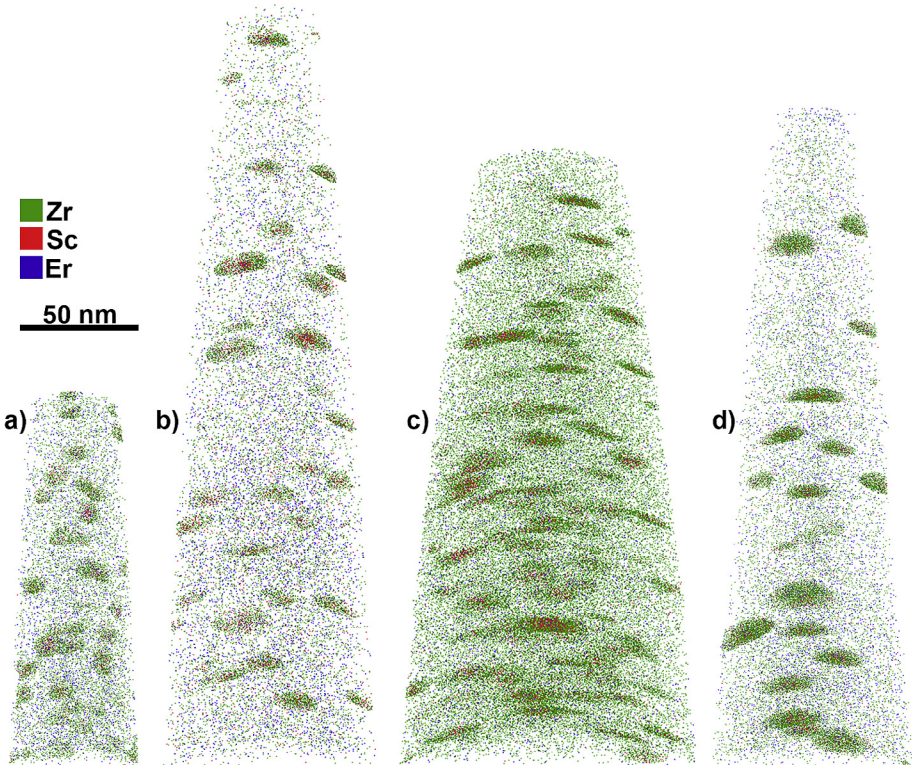

Fig. 3. Three-dimensional (3-D) APT reconstructions of Al-0.08Zr-0.014Sc-0.008Er-0.10Si at.% (*low Sc alloy*) isothermally aged at 375 °C for a) 24 h and b) 21 days or at 400 °C for c) 24 h and d) 11 days, after being homogenized for 8 h at 640 °C. Scandium atoms are displayed in red, Zr atoms in green, Er atoms in blue. Al and Si atoms are omitted for clarity.

Table 2
Precipitate number density, N_V, mean radius $\langle R \rangle$, volume fraction, φ, and microhardness, HV, for Al-0.055Sc-0.005Er-0.02Zr-0.05Si at.% (*high Sc alloy*) [26] homogenized 2 h at 640 °C and isothermally aged at 400 °C for 0.5 or 66 days, for Al-0.055Sc-0.005Er-0.02Zr-0.18Si at.% (*higher Si alloy*) [29] homogenized 2 h at 640 °C and isothermally aged at 400 °C for 0.5 or 2 h, and for Al-0.08Zr-0.014Sc-0.008Er-0.10Si at.% (*low Sc alloy*) homogenized 8 h at 640 °C and isothermally aged at 375 °C for 24 h or 21 days, or aged at 400 °C for 24 h or 11 days.

Alloy's composition	Aging	N_V ($\times 10^{22}$ m^{-3})	$\langle R \rangle$ (nm)	ϕ (%)	HV (MPa)
Al-0.055Sc-0.005Er-0.02Zr-0.05Si	400 °C/0.5 h	1.11 ± 0.37	4.1 ± 0.8	0.235	504 ± 13
	400 °C/66 days	0.2 ± 0.10	6.3 ± 0.3	0.210	429 ± 14
Al-0.055Sc-0.005Er-0.02Zr-0.18Si	400 °C/0.5 h	2.23 ± 0.57	2.9 ± 0.7	0.229	536 ± 16
	400 °C/2 h	1.94 ± 0.27	3.1 ± 0.9	0.252	607 ± 9
Al-0.08Zr-0.014Sc-0.008Er-0.10Si	375 °C/24 h	9.21 ± 0.59	1.9 ± 0.4	0.31 ± 0.02	628 ± 20
	375 °C/21 days	2.22 ± 0.26	2.7 ± 0.7	0.34 ± 0.04	566 ± 22
	400 °C/24 h	3.56 ± 0.34	2.7 ± 0.6	0.33 ± 0.03	575 ± 35
	400 °C/11 days	1.69 ± 0.44	3.4 ± 0.7	0.37 ± 0.09	515 ± 18

with data obtained from the a *high Sc alloy* (Al-0.055Sc-0.005Er-0.02Zr-0.05Si) [26] and a high Sc alloy with a *higher Si* concentration (Al-0.055Sc-0.005Er-0.02Zr-0.18Si) [29]. The *low Sc alloy* displays a surprisingly high number density of nanometric size precipitates, with a maximum measured number density of $1.29 \pm 0.2 \times 10^{23}$ m^{-3}, obtained in a nanotip aged 24 h at 375 °C, and displays a high volume fraction (ϕ) of precipitates, estimated to be between 0.3 and 0.35%. In comparison, the two Sc-rich alloys have only a volume fraction of 0.21–0.25% and a number density between 1 and 2×10^{22} m^{-3} for peak aging conditions at 400 °C. For this same aging temperature and at a peak age condition (24 h), the *low Sc alloy* displays a number density of $3.56 \pm 0.34 \times 10^{22}$ m^{-3}, which represent a two to four-fold increase when compared to the two prior alloys. For the peak aging conditions, the mean precipitate radius is 1.9 ± 0.4 nm at 375 °C and 2.7 ± 0.6 nm at 400 °C for the *low Sc alloy*. In the peak aged condition at 400 °C, the *high Sc alloy* has a mean precipitate radius of 4.1 ± 0.8 nm, whereas for the *higher Si alloy* it is 3.1 ± 0.9 nm.

During aging of the *low Sc alloy*, the precipitate number density decreases by a factor of four in 20 days at 375 °C, while simultaneously the precipitates's mean radius increases by 0.8 nm, reaching 2.7 ± 0.7 nm. At 400 °C, the number density decreases by ~50% and the precipitates's mean radius increases by 0.7 nm over 10 days (3.4 ± 0.5 nm). For the *high Sc alloy* aged at 400 °C, the number precipitate density decreases to $0.2 \pm 0.1 \times 10^{22}$ m^{-3} over 65 days, while the precipitates's mean radius increases by 2.2 nm–6.3 ± 0.3 nm. The overaged data for the *higher Si alloy* were estimated based on microhardness values measured on a sample aged 65 days at 400 °C (381 ± 11 MPa). A precipitate number density of $7 \pm 3 \times 10^{20}$ m^{-3} and mean precipitate radius of 12.5 ± 2.5 nm were estimated.

Proximity histograms are displayed in Fig. 4, showing the radial concentration profiles of the precipitates at a given distance from the average α-Al/(Al,Si)$_3$(Sc,Zr,Er) interface, defined by an isoconcentration surface at the inflection point of the Al concentration profile. These specific concentration profiles have been measured using the datasets displayed in Fig. 3. Zirconium and Sc concentration profiles are displayed according to the left-hand ordinate, while Er and Si are displayed according to the right-hand ordinate. Representative precipitates for each aging conditions are displayed in the insets; the scale mark is 10 nm long. The precipitates exhibit core-shell structures, with a shell that is close to Al_3Zr and a core enriched in Sc, Er and Si. In the peak aged condition at 375 °C (a), relatively steep concentration profiles are measured inside the nanoprecipitates. For this configuration, the core radius and shell thickness are about 1 nm. After 21 days at 375 °C (b), the nanoprecipitates grow and the concentration gradients inside the nanoprecipitates exhibit some flattening, indicating that the core-shell structure is progressively homogenizing, while simultaneously more Zr atoms are incorporated, progressively replacing Sc and Er atoms in the core. For an aging temperature of 400 °C, at peak-aged conditions (c), the precipitates display a large Sc-Er-Si enriched core, about 2 nm radius, surrounded by a 1.5 nm thick Zr-enriched shell. Note that a diffuse core-shell interface is observed. When the nanoprecipitates are aged at 400 °C 11 days (d), the concentration profiles become homogenized and the enriched core shrinks to about 0.5 nm while the shell grows. The initial formation of a Zr-enriched shell was anticipated due to the smaller diffusivity of this element in aluminum, when compared to the diffusivities of Sc and Er in Al; hence these two elements precipitate first. The nearly pure Al_3Zr shell was, however, an unexpected feature of the nanoprecipitates. Indeed, the previously investigated Al-Sc-Er-Zr-Si alloys only displayed an enrichment of Zr in the shell, with a maximum observed Zr concentration of ~7 at.% after 66 days of aging at 400 °C [26], whereas the

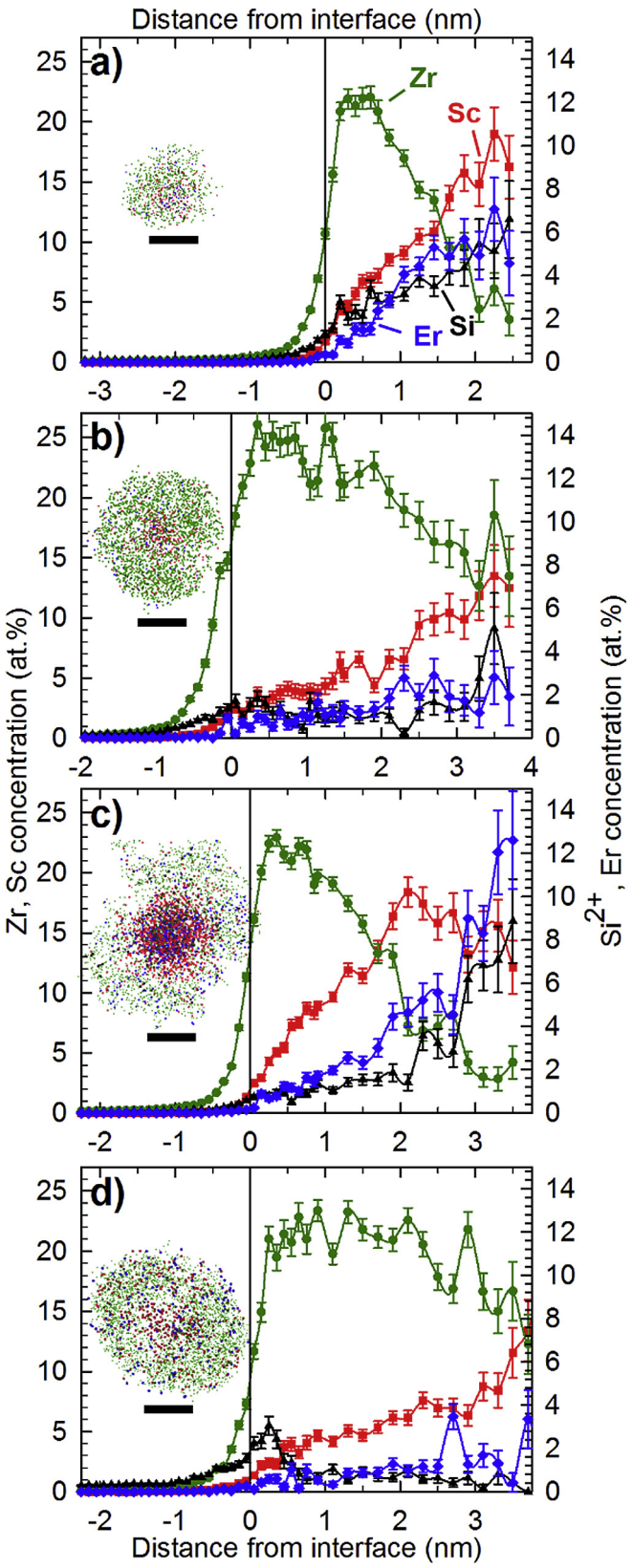

Fig. 4. Concentration profiles across matrix/precipitate interfaces of Al-0.08Zr-0.014Sc-0.008Er-0.10Si at.% (*low Sc alloy*) isothermally aged at 375 °C for: (a) 24 h; (b) 21 days or at 400 °C; (c) 24 h; and (d) 11 days, after being homogenized for 8 h at 640 °C. The inset images show 3-D APT reconstructions of representative precipitates. Scandium atoms are displayed in red, Zr atoms in green, Er atoms in blue and Si in black. The black scale markers are 10 nm long.

nanoprecipitates already exhibit a 1.5 nm thick Al_3Zr shell after 24 h at 400 °C.

As shown in Table 3, this higher Zr concentration can also be easily observed for the average precipitates's composition. For the previously developed alloys (*high Sc* and *higher Si* alloys), the nanoprecipitates exhibited high Sc concentrations (~21%) and small concentrations of Zr (0.3–1.4%) and Er (~2%) for the peak aged condition. As the nanoprecipitates grow, the Zr concentration increases, with a maximum concentration of 3.46%. For the *low Sc alloy*, the main constituent of the nanoprecipitates is Zr (~20 at.%) with only 4–7 at.% Sc and 1–2 at.% Er. Our new alloy thus displays a complete shift from Sc to Zr as the main constituent of the nanoprecipitates. Since the Er concentration in the alloys is essentially the same, the mean nanoprecipitate concentration of Er hasn't been modified. A more important difference can be observed concerning the Si concentration. Silicon has previously been shown to partition to inside the nanoprecipitates. For example, in the *high Sc alloy*, which contains 0.05 at.% Si, the concentration of Si inside the nanoprecipitates lies between 1.1 and 2.8 at.%, whereas it increases to 5–5.8 at.% for the *higher Si alloy*, with 0.18 at.% Si. For the *low Sc alloy*, which contain 0.1 at.% Si, the Si only represents 1.2–2.7% of the nanoprecipitates's mean composition, comparable to the *high Sc alloy*. This limited incorporation of Si into the nanoprecipitates, compared to the overall Si present in the matrix, suggests a weaker interaction energy between Si and Zr atoms than between Si and Sc atoms. Interestingly, we observe that for long aging durations (mean value between sample aged 21 days at 375 °C and 11 days at 400 C) (Table 3) the Zr:Sc:Er atomic ratio in the nanoprecipitates is 80:16.5:3.5, which is similar to the mean Zr:Sc:Er ratio in the alloy with an overall ratio of 81.7:14.9:3.4 as determined by LEAP tomography (Table 1). Although solute concentrations may fluctuate from nanotip-to-nanotip, during APT analyses, due to the dendritic structure and the small analyzed volumes, the local precipitate composition ratios always follow the overall nanotip's composition.

Table 3 also displays the mean matrix compositions measured from several analyzed LEAP tomographic volumes. As we have observed, most of the expensive Sc is partitioning to the precipitates, and only ~10 at ppm Sc remains in the matrix of the *low Sc alloy* at peak aging, and is as small as ~5 at ppm for long aging times, whereas the Sc-rich alloys exhibit high amounts of Sc (50–70 at ppm) in the matrix. The same trend is observed for the Zr matrix concentration. For peak aging conditions, the *low Sc alloy* displays a small concentration of Zr solute remaining in the matrix (~150 at ppm at peak aging), which decreases further during aging (~30 at ppm for both overaged condition at 375 °C and 400 °C). No peaks associated with Er isotopes are detected in the mass spectrum of the *low Sc alloy*'s matrix. In contrast to these three solute species Si does not partition strongly to the nanoprecipitates, rather it remains dissolved in the matrix. From the total of 1000 at ppm of solute atoms (Sc, Er and Zr), after peak aging, respectively, at 375 °C and 400 °C, only 152 and 164 at ppm, respectively, of these solutes remain in the matrix, which means that more than 85% of the solute atoms precipitate, whereas only one third of the 800 at ppm solute atoms precipitate for the *high Sc alloys*. The higher total solute-atom concentrations result in increased partitioning of solute elements to the nanoprecipitates and to an increased volume fraction of $L1_2$ nanoprecipitates and therefore higher microhardness values.

3.3. Creep behavior at 300 °C

To investigate the effects of the nanoprecipitates's size on the creep strength, samples of the new *low-Sc alloy* were either annealed up to peak conditions at 375 °C for 24 h (~628 MPa), or overaged at 400 °C for 11 days (~515 MPa). Since the microstructures of the alloy after these two different aging conditions have been investigated by LEAP tomography, the initial average radius of nanoprecipitates *prior* to creep is known (1.9 and 3.4 nm, respectively). As the creep experiments are performed at 300 °C, well below the aging temperature, no significant coarsening of the nanoprecipitates occurs during creep deformation. A typical compressive creep strain vs. time curve is shown in Fig. 5a. For this particular test performed on a peak-aged sample, the compressive creep experiment commenced with an applied stress of 18 MPa and, once the minimum strain rate was achieved for a given stress, the load was increased further, up to a stress of 21.8 MPa; the experiment was terminated when a total strain of 10% was achieved. The blue line indicates the measured slopes when a minimum strain rate was achieved. Fig. 5b displays a double-logarithmic plot of the minimum compressive creep strain-rate versus applied stress during a creep experiment at 300 °C for the Al-0.08Zr-0.014Sc-0.008Er-0.10Si alloy (*low Sc alloy*). Data concerning Al-0.08Sc, Al-0.06Sc-0.02Er and Al-0.06Sc-0.02Zr, see Refs. [8,37], are included for comparison.

For both aging conditions, the *low Sc alloy* exhibits significant creep resistance at 300 °C, similar to the binary Al-0.08Sc alloy, which has four times more Sc. High apparent stress exponents are observed ($n_{ap} = 36 \pm 1$), which are indicative of a threshold stress, below which creep is not measurable. A modified version of the Mukherjee-Bird-Dorn power-law equation states that the minimum strain rate $\dot{\varepsilon}$ is given by:

$$\dot{\varepsilon} = A(\sigma - \sigma_{th})^n \exp\left(\frac{-Q}{k_B T}\right) \quad (1)$$

where A is a constant, σ is the applied stress, σ_{th} is the threshold stress, n is the matrix stress exponent, Q is the matrix creep activation energy, k_B is the Boltzmann constant and T the absolute temperature. The value of the threshold stress, σ_{th}, is calculated by dividing the intercept by the slope employing a weighted least-squares linear-regression analysis of $\sqrt[n]{\dot{\varepsilon}}$ versus σ [38]. The experimental value for the Al matrix, $n = 4.4$, is employed [39]. Threshold

Table 3
Composition of nano-precipitates and the matrix in the same three alloys listed in Table 2.

Alloy's composition	Aging	Precipitates comp. (at. %)					Matrix comp. (at. ppm)			
		Al	Sc	Er	Zr	Si[a]	Sc	Er	Zr	Si[a]
Al-0.055Sc-0.005Er-0.02Zr-0.05Si	400 °C/0.5 h	73.3	21.4	2.2	0.3	2.8	76	21	157	274
	400 °C/66 days	74.2	19.5	1.7	3.5	1.1	49	14	14	441
Al-0.055Sc-0.005Er-0.02Zr-0.18Si	400 °C/0.5 h	74.5	16.7	1.6	1.4	5.8	63	4	242	845
	400 °C/2 h	70.1	21.0	1.7	2.2	5.0	55	ND	72	902
Al-0.08Zr-0.014Sc-0.008Er-0.10Si	375 °C/24 h	71.9	6.6	2.2	16.7	2.6	11	ND	141	878
	375 °C/21 days	73.0	3.7	1.0	21.1	1.2	5	ND	31	880
	400 °C/24 h	72.7	7.0	1.6	17.5	1.2	10	ND	154	763
	400 °C/11 days	73.5	4.7	0.8	19.8	1.2	5	ND	30	917

[a] Atomic concentration of $^{28}Si^{2+}$ in LEAP tomographic mass spectrum.

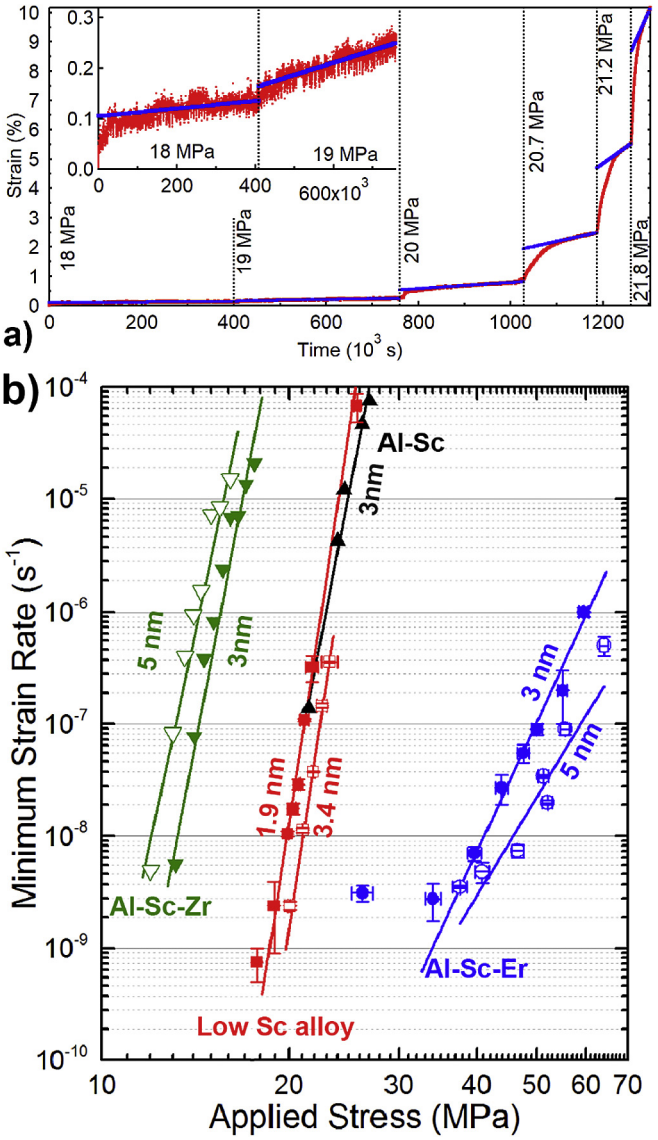

Fig. 5. a) Strain vs. time for compressive creep of the *low Sc alloy*, homogenized at 640 °C for 8 h and peak-aged at 375 °C for 24 h. The inset is a magnification of the low strain rate region. The straight lines indicate the minimum strain rates. b) Double-logarithmic plot of minimum compressive creep strain-rate vs stress for a creep test at 300 °C of the Al-0.08Zr-0.014Sc-0.008Er-0.10Si alloy at.% (*low Sc alloy*), homogenized at 640 °C for 8 h, then aged at 375 °C for 24 h (1.9 nm) or aged at 400 °C for 11 days (3.4 nm). Data for Al-0.08Sc, Al-0.06Sc-0.02Er and Al-0.06Sc-0.02Zr, from Refs. [8,37], are included for comparison.

stresses of 17.5 ± 0.6 MPa and 19.3 ± 0.6 MPa are determined using the data obtained during creep of samples, which had been, respectively, peak aged or overaged.

4. Discussion

4.1. Modeling of strength

To identify the operating strengthening mechanism in this alloy, the strength increment induced by different possible mechanisms are calculated: (i)ordering strengthening (σ_{ord}); (ii) coherency and modulus strengthening ($\sigma_{coh} + \sigma_{mod}$); and (ii) Orowan dislocation looping (σ_{oro}). The associated equations are given in Appendix A, which, together with the present discussion, follow prior similar discussions on high-Sc alloys [3,4,15,17,20,26]. The estimated strength increments are reported in Table 4 and compared with the experimentally obtained strength increment, defined as ΔHV/3 [40]; ΔHV is the difference between the measured microhardness of the precipitation strengthened alloy and the microhardness of pure Al, 200 MPa [7,16,41]. In Fig. 6 the calculated strength increment is plotted as a function of the nanoprecipitates's mean radius, for two volume fractions, 0.3% and 0.35%, in addition to the experimentally obtained strength increments for the four conditions investigated by LEAP tomography. The critical mean nanoprecipitate radius between coherency plus modulus strengthening and Orowan strengthening is estimated to be at ~2.2 nm, at which point nanoprecipitate bypassing becomes the limiting factor.

For the peak aged conditions at 375 °C, a mean nanoprecipitate radius of 1.93 ± 0.42 nm, a volume fraction of 0.31% and a strength increment of 142 ± 7 MPa were measured. For this nanoprecipitate mean radius and volume fraction, the strengthening mechanism appears to be coherency and modulus strengthening with an estimated value of 150 ± 15 MPa. The microstructures after aging at 375 °C for 21 days or at 400 °C for 24 h are extremely similar ($\langle R(t = 21 \text{ days or } 24 \text{ h})\rangle = 2.7$ nm, and $\phi = 0.34$ or 0.33%), which give rise to similar strength increments (122 ± 7 or 125 ± 12 MPa). As displayed, however, in Fig. 6, the calculated Orowan strength increment is somewhat overestimated for both cases. The same is true for the sample aged 11 days at 400 °C with $\langle R(t = 11 \text{ days})\rangle = 3.4 \pm 0.7$ nm, with a measured strength increment of 105 ± 6 MPa. Although within the range of the error bars, this lower experimental value (105 ± 6 MPa) suggests a lower effective volume fraction than the one determined by atom-probe tomography, which may be related to the effects of the dendritic structure on the distribution of solute atoms and thus on the distribution of nanoprecipitates. As previously demonstrated [30], the Zr distribution is inhomogeneous after solidification of the alloy, which displays dendritic cores enriched in Zr, and interdendritic channels depleted in Zr. Unlike for Er, Sc and Si, the slow diffusivity of Zr does not permit to fully homogenize the solute, even after annealing at 640 °C for 24 h. Furthermore, large Al_3Zr precipitates form during this homogenization annealing step, thereby depleting the matrix of Zr. Due to this segregation of Zr, interdendritic channels depleted of $L1_2$ nanoprecipitates are formed in the interdendritic regions. The nanoprecipitate-free channels are relatively narrow (~15 μm channels vs. >100 μm cores [30]), therefore the probability to prepare randomly a nanotip containing a channel is small. The overall volume fraction across the dendritic structure (channel and dendrites) is thus expected to be smaller than was measured by LEAP tomography, which would explain the difference in microhardnesses between simulations and measurements. Unaffected by this sampling issue the study of the precipitate sizes distribution (Fig. 6) indicates that the peak aged condition at 375 °C is close to the transition point between dislocation shearing and dislocation looping of nanoprecipitates and both mechanisms could be operational due to the spatial distribution of nanoprecipitates and their size distributions (as studied via dislocation dynamics modeling [42]), whereas for longer aging times (and large precipitate mean radius, the Orowan looping mechanism occurs and limits the alloy's microhardness.

4.2. Nanoprecipitation kinetics

In the previously investigated Al-Sc-Er-Zr alloys with high Sc-concentrations, the precipitation of Sc atoms was the main source of strengthening [17], which allowed to reach the peak microhardness after only 30 min of aging at 400 °C due to the large diffusivity of Sc and/or Er. The controlled addition of Si [26,29] further reduced this incubation time to 10 min, while simultaneously increasing the microhardness of the alloy due to an

Table 4
Experimental (ΔHV/3) and calculated strength increments (eq. (A1–A4) for the *low Sc alloy*.

Alloy's composition	Aging	Strength Increment (MPa)			
		$\Delta\sigma_{ord}$	$\Delta\sigma_{coh} + \Delta\sigma_{mod}$	$\Delta\sigma_{Or}$	ΔHV/3
Al-0.08Zr-0.014Sc-0.008Er-0.10Si	375 °C/24 h	131 ± 13	150 ± 15	168 ± 17	142 ± 7
	375 °C/21 days	137 ± 14	174 ± 17	143 ± 14	122 ± 7
	400 °C/24 h	134 ± 13	168 ± 17	141 ± 14	125 ± 12
	400 °C/11 days	142 ± 14	186 ± 19	129 ± 13	105 ± 6

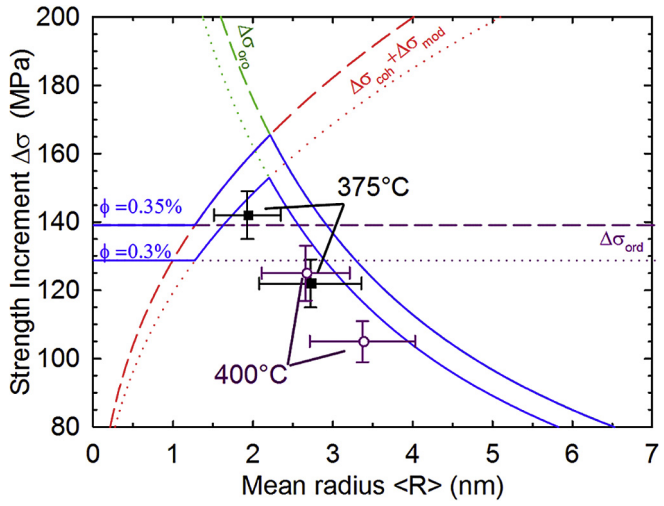

Fig. 6. Yield stress increment vs. mean precipitate radius, ⟨R⟩, for the *low Sc alloy* (Al-0.08Zr-0.014Sc-0.008Er-0.10Si at.%) aged at 375 °C for 24 h or 21 days (black squares), or aged at 400 °C for 24 h or 11 days (open circles). The curves represent calculated predictions of the strength increment associated with ordering (purple) (eq. (A1)), coherency and modulus (red) (eq. (A2 and A3) or Orowan (green) (eq. (A4)) strengthening for volume fractions ϕ of 0.3% (dotted line) and 0.35% (dashed line).

increased number density of nanoprecipitates and their volume fraction. The acceleration of solute diffusivities is due to an attractive interaction of Si atoms with Sc and Zr atoms; the respective binding energies are 0.33 and 0.18 eV atom^{-1} at first nearest-neighbor sites. Additionally, Me-Si-V trimers form due to attractive binding energies and they have an enhanced mobility [19]. Alternatively, due to Zr's small diffusivity in Al, the Zr-rich alloys need excessively long aging times before achieving a peak microhardness [10,11,18,22,23], generally more than 100 h at 400 °C for a similar concentration of solute used in this study. As for Al-Sc based alloy, addition of Si to Al-Zr based alloys induces faster precipitation kinetic [23,43–45].

In our *low Sc alloy*, even though Zr is the main solute element, the relatively high Si concentration enables achieving peak microhardness after a short time of 24 h at 400 °C (cf. Fig. 2a), which is a significant reduction of time compared to the 100 h needed for an Al-0.1Zr alloy aged at 400 °C (microhardness is ~420 MPa). This strong reduction cannot, however, be assigned solely to the addition of Si [23,43–45] as the addition of Sc [15,16] and Er [18,22] also reduce the time necessary to reach peak microhardness by forming *nuclei* on which the Zr atoms precipitates. The faster precipitation kinetics thus results from a synergistic effect among these elements.

4.3. Apparent activation energy for precipitation

As noted, following the change in electrical conductivity or its reciprocal, electrical resistivity, allows to monitor the precipitation of solute from the matrix. The scattering of electrons by solute atoms in the matrix is stronger than their scattering by precipitates. At a low defect concentration, the increase in resistivity is proportional to the concentration of an impurity. For example, in the case of Sc in aluminum, the electrical resistivity, ρ, increases by 34 nΩ m per atomic % [46]. Due to the presence of four impurities in our alloy (Sc, Er, Zr and Si) each with its own scattering cross-section, it is not possible to monitor precisely the change in matrix composition from the electrical resistivity curves and obtain solubility limits. Analyzing such curves can, however, yield an apparent activation energy for precipitation using the cross-cut method [47].

To apply the cross cut-method, isothermal annealing must be applied to a set of identical samples, that is, after homogenization. By drawing a line parallel to the time axis at a given value of resistivity, ρ_n, the time needed, t_i, to achieve a specified change in solute concentration at a temperature, T_i, can be measured. If several isothermal annealing curves are utilized, the temperature dependence of the time needed to achieve a specified change of resistivity is described by:

$$\ln(t_i) = I n\xi + \frac{Q_{app}}{k_B T_i} \quad (2)$$

where Q_{app} is the apparent activation energy for precipitation and k_B is Boltzmann's constant. The logarithm of t_i is thus linear in $1/T_i$ with a slope of Q_{app}/k_B. By using several different cuts, one can check that a single thermally activated process is occurring. If a constant activation energy is operative in the investigated temperature range, all lines should be parallel and only offset by ξ.

For easier reading, Fig. 7a shows the relative resistivity change in percent, %, as a function of aging time, calculated from the measured electrical conductivity curves (Fig. 1b). Several cuts were made to obtain a precise value of the apparent activation energy and check that it is a singly thermally activated process. Fig. 7b is a plot of the logarithmic variation of t_i as a function of $1000/T_i$ for different specified values of resistivity changes. Fig. 8 displays the activation energy obtained from the slope of those curves. An apparent activation energy of 0.66 ± 0.14 eV was determined in the rapid growth region (less than 10% resistivity change) and this is in good agreement with 0.70 ± 0.09 eV, which was previously obtained from the isochronal annealing experiments [30].

Deviations from this value are observed for a resistivity change greater than 10% (cf. Fig. 8). Beyond the 24 h mark (cf. Fig. 7b)., application of the cross-cuts method does not yield a constant slope in the investigated temperature range, which indicates that another thermally-activated process is occurring. Although the cross-cuts made at values of 12.75%–13.25% exhibit a constant slope versus 1000/T (cf. Fig. 7b), they are not parallel to each other, leading to a variation in the apparent activation energy (from 1.9 ± 0.06 to 1.7 ± 0.14 eV) (Fig. 8). The estimated apparent activation energy for a resistivity change greater than 10% represents a convolution of multiple processes whose physical meaning is difficult to ascertain from the experiments performed. Due to the change in solid-solubility as a function of temperature, the matrix composition exhibits different equilibrium concentrations, as indicated by the

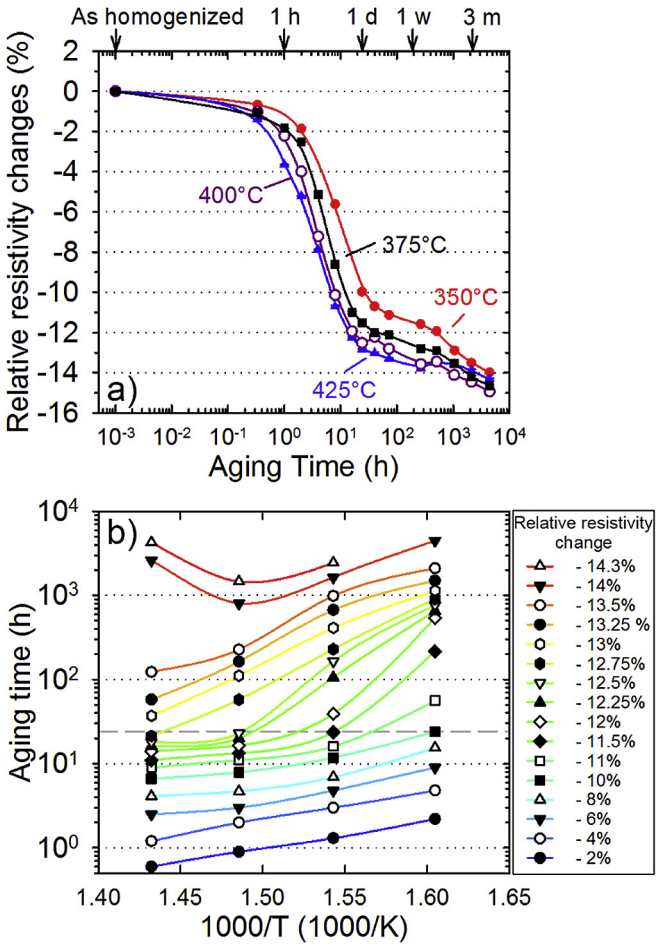

Fig. 7. a) Evolution of the relative resistivity change during isothermal aging at 350 °C (solid circles), 375 °C (solid squares), 400 °C (open circles) and 425 °C (solid triangles) of the *low Sc alloy* (Al-0.08Zr-0.014Sc-0.008Er-0.10Si at.%) homogenized at 640 °C for 8 h. (b) Variation of the time needed to reach a defined resistivity change, as a function of the reciprocal of the aging temperature (1000/K). The dashed line represents an aging time of 24 h.

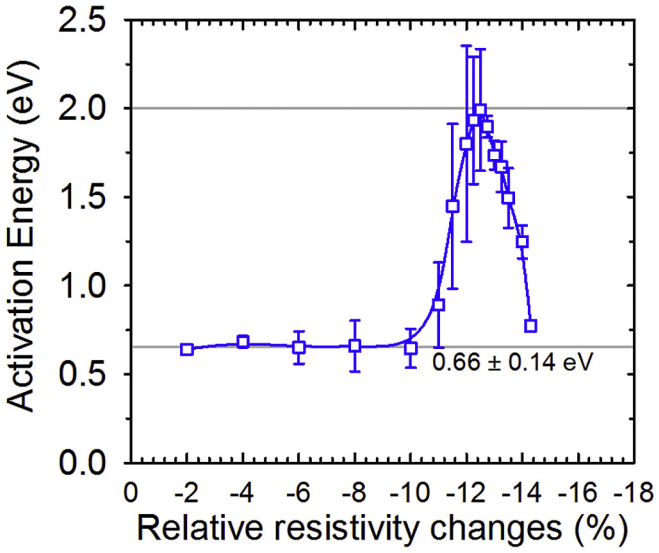

Fig. 8. Change in the effective activation energy as a function of relative resistivity change during isothermal aging experiments, as estimated utilizing the method of cross-cuts [47].

crossing resistivity curves. Thus, it is not possible to determine a diffusion-limited activation energy using the above approach. However, according to the Lifshitz-Slyozov-Wagner (LSW) model, if coarsening of precipitates is diffusion-limited, the matrix composition should evolve according to the following equation:

$$\Delta C(t) = C(t) - C(\infty) = \kappa(t - t_0)^r \quad (3)$$

where t_0 is the onset of the quasi-stationary coarsening regime, C(t) the matrix composition, C(∞) the equilibrium concentration, κ the rate constant and r the temporal exponent. Since ρ is proportional to C, the change in resistivity during diffusion-limited coarsening follows:

$$\Delta\rho(t) = \rho(t) - \rho(\infty) = K^*(t - t_0)^r \quad (4)$$

According to the LSW model, the temporal exponent r is $-1/3$ when coarsening is diffusion-limited. Using a nonlinear multivariate regression analysis [48], K, $\rho(\infty)$ and r were fitted using the resistivity curves for a time greater than 264 h and for all four temperatures, separately. A temporal exponent r of $-1/3$ is obtained each time, confirming that the long-term coarsening behavior of the $L1_2$ $(Al,Si)_3(Sc,Er,Zr)$ nanoprecipitates is indeed diffusion-limited.

4.4. Coarsening resistance

In previous work on a high-Sc concentration Al-Sc-Er-Zr alloy [17], it was demonstrated that the coarsening of the nano-precipitates was extremely slow over extended time periods, the microhardness value being stabilized at ~450 MPa for aging 64 days at 400 °C, before slowly decreasing. As previously discussed, the addition of 0.05 at.% Si induced faster precipitation kinetics and also increased the peak microhardness value [26]. However, it had the undesirable effect of causing faster coarsening of the nano-precipitates; the alloy's microhardness decreased after 3 days at 400 °C. The long-term microhardnesses of the alloy was, however, comparable to the Si-free alloy beyond 12 days, displaying similar decreasing rates. Further increasing the Si concentration in the alloy accentuated these effects, leading to higher microhardnesses and faster over-aging kinetics [29].

The same effect is anticipated to occur in the *low Sc alloy*. As shown in Table 3, most of the nano-precipitate-forming solute atoms have already precipitated for the peak-aged conditions. A longer aging time allows more solute atoms to precipitate from the matrix but it has a limited effect on the volume fraction. This thus cannot account for the observed increase in the precipitate mean radius (cf. Table 2). A significant decrease in number density is, however, observed indicating coarsening of the nano-precipitates caused by Ostwald ripening. Due to the small partitioning of Si into the nano-precipitates, the Si atoms remain in solid-solution in the matrix (cf. Table 3). These atoms remain available to enhance the diffusion kinetics of Zr, Sc and Er atoms. Since the precipitate growth rate is proportional to the solute diffusivity during Ostwald ripening [49]; the high concentration of Si in the matrix reduces the coarsening resistance of the nano-precipitates. It is anticipated that further increasing the Si concentration in this *low Sc alloy* will induce faster precipitation kinetics, reducing the time to achiever the peak aging state, and increase peak microhardness. However it would also further reduce the coarsening resistance of the alloy, as in the Sc-rich Al-Sc-Er-Zr-Si [29].

Nevertheless, the *low Sc alloy* exhibits higher strength than the prior alloys for extended lengths of time at 400 °C, and it displays the same strength as the *high Sc* [26] and Al-Sc-Er-Zr [17] alloys after 1000 h (Fig. 2a). Although the *low Sc alloy* achieve a smaller

peak microhardness compared to the *high Sc alloy* when aged directly at 425 °C (Fig. 2b), it displays a slightly slower loss of microhardness during further aging, most probably due to the formation of the more stable and thicker Al_3Zr shell.

4.5. Creep properties

The *low Sc alloy* exhibits the same creep resistance as the Sc-richer Al-0.08Sc binary alloy (cf. Fig. 5b), which can be explain by considering the precipitates's compositions. Creep resistance in Al-Sc-based alloys has been shown to depend on mean precipitate radius and the lattice parameter mismatch strains between the $L1_2$ precipitates and the matrix [8]. Due to the complex core/shell structure of the nanoprecipitates, whose compositions and size ratios evolve with aging time, we calculate, as an approximation, the $L1_2$ precipitate lattice parameter using Vegard's rule, when considering the average nano-precipitate composition (Table 3). Possible effects of the core/shell structure's homogenization, during aging, on lattice parameter mismatch are not considered. An average lattice parameter of 4.093 ± 0.03 Å is calculated using the lattice parameters a of Al_3Zr, Al_3Sc and Al_3Er [50]. The lattice parameter mismatch between precipitate and matrix is 1.1% at ambient temperature. It is anticipated that the nano-precipitates formed in the *low Sc alloy* induces a strain field similar to the one produced by stoichiometric coherent Al_3Sc precipitates (a = 4.103 Å). In comparison with the threshold stresses of 17.5 ± 0.6 and 19.3 ± 0.6 MPa obtained for the *low Sc alloy* (Fig. 5b), Al-0.08Sc alloy exhibits σ_{th} = 19.8 ± 1.3 MPa for a mean precipitate radius of 3 nm and, Al-0.06Sc-0.02Er threshold stresses of 17 ± 1 and 22 ± 1 MPa for mean precipitate radii, respectively, of 3 nm and 5 nm [8]. For the Al-0.06Sc-0.02Zr alloy, with nano-precipitates exhibiting a smaller mismatch than Al_3Sc due to the Zr addition, as the nanoprecipitates grew from 3 to 5 nm, the threshold stress decreased from 12.4 ± 0.3 to 11.3 ± 0.3 MPa [37]. The *low Sc alloy* thus displays threshold stresses close to those of Al-Sc and Al-Sc-Er alloys and much higher than that of Al-Sc-Zr. The reduced creep strength anticipated for the Al_3Zr smaller lattice parameter mismatch is thus compensated, in the *low Sc alloy*, by the Sc- and Er-enriched core, which induce a larger lattice parameter mismatch with the surrounding matrix. As the precipitates grow larger, a stronger strain field is created, thereby further impeding dislocation motion. The *low Sc alloy*'s creep resistance improves as the mean precipitate radius increases. As seen in Fig. 5b, for a given stress, the minimum strain rate is almost ten times slower for the overaged condition when compared to the peak aging condition.

4.6. Nano-precipitates's concentration profiles

Concentration profiles within precipitates formed in the Al-Sc-Er-Zr alloys exhibited a core-double shell structure with an Er-enriched core, Sc-rich inner-shell and Zr-rich outer-shell [17]. The concentration profiles were estimated to result from the sequential precipitation of Er, Sc and Zr due to their different intrinsic diffusivities in aluminum ($D_{Er} > D_{Sc} > D_{Zr}$). Due to the small diffusivities of solute in the $Al_3X(L1_2)$ nano-precipitates, the concentration profiles were maintained for extended aging durations [17]. Addition of Si to the quaternary alloy induces the formation of a homogenized mixture of Sc, Er and Si atoms in the core and a Zr rich shell [26,29]. It was proposed that the Si addition induces the formation of Si-Er and Si-Sc dimers; these dimmers could have similar diffusivities in the aluminum matrix, thus preventing the sequential precipitation of Er and Sc. Another proposed scenario is the possibility that Si additions in the $L1_2$ precipitates's cores could enhance the diffusivities of Sc and Er inside the nano-precipitates, which reduce the concentration gradients.

LEAP tomographic investigations performed on the *low Sc alloy* revealed that the $L1_2$ precipitates's concentration profiles were strongly affected by the drastic change in the alloy's composition. Table 3 shows that, besides aluminum, the main constituent in Sc-rich alloys was Sc with an average precipitate composition close to 20 at.% Sc and only 2–3 at.% Zr at peak aged conditions, whereas the new alloy displays nearly opposite concentrations of Zr and Sc (16–20% Zr and 3–7% Sc). This is due to the formation of a small Sc, Er, Zr and Si core surrounded by a thick Zr shell (cf. Fig. 4). An interesting feature of these precipitates is the smaller partitioning of Si in the new alloy compared to the alloys with higher concentration of Sc. This phenomenon confirms a previously *ab initio* calculated site substitution energies Si inside Al_3X structures [19]. The site substitution energy of Si on an Al sublattice site in Al_3Sc and Al_3Zr, were, respectively, estimated to be 1.33 eV and 0.66 eV. In comparison to previous alloys, it is assumed that the lower concentration of Si that partition the precipitate is correlated with the reduced concentration of Sc per nano-precipitate.

Long aging times induces homogenization of the precipitates's concentration profiles (Fig. 4), progressively reducing the concentration gradients between the core and the shell of the nano-precipitates. This homogenization is possibly due to the aforementioned Si effect on solute diffusivities inside the nano-precipitates but also due to the large Zr concentration gradients.

5. Conclusions

The properties of a new low-Sc concentration and high-Zr concentration aluminum alloy, Al-0.08Zr-0.014Sc-0.008Er-0.10Si (at.%), designed to minimize the concentration of the expensive element scandium, while maintaining the desirable strengthening provided by precipitation of coherent tri-aluminide $L1_2$ nanoprecipitates, were investigated employing microhardness, electrical conductivity, compressive creep, scanning electron microscopy (SEM) and atom-probe tomography (APT). Based on the experimental results obtained, we conclude that reducing the cost of Al-Zr-Sc-Er-Si alloys can be achieved by replacing the expensive element Sc by the much less expensive element Zr; specifically, utilizing only one-quarter of the original Sc concentration and compensating for it by increasing the Zr concentration by a factor of four. The following conclusions are deduced from the experimental results:

1. Isothermal aging performed between 350 and 425 °C, for times up to six months, demonstrate that a high microhardness can be achieved in a relatively short period of time, only 24–40 h, as compared to >100 h for Sc-free Al-Zr alloys. An aging temperature of 375 °C provides a high microhardness, while maintaining a reasonably short aging time.
2. The new alloy displays a similar peak microhardness as the Al-0.055Sc-0.005Er-0.02Zr-0.10Si at.% alloy when aged at 400 °C (575 ± 35 MPa). It, however, does not suffer from the rapid coarsening of nanoprecipitates due to the high Si concentration and remains as strong as the Si-free Al-Sc-Er-Zr alloy for at least six months.
3. The high strength achieved is due to the high number density of nano-precipitates that are nucleated (close to 10^{23} m^{-3}), and thus a high volume fraction is achieved (0.3–0.35%). These $(Al,Si)_3(Sc,Zr,Er)$ $(L1_2)$ nanoprecipitates display initially a core-shell structure; the core being a mixture of Sc, Zr, Er and Si atoms, surrounded by a shell consisting of Al_3Zr containing a small amount of Sc, Er and Si. During aging, the core-shell structure is continuously being homogenized. The mean nano-precipitates's composition, determined by APT, demonstrates that Zr is the main constituent and it accounts for ~20%, followed by Sc (4%) and Er (1%).

4. The weak partitioning of silicon to the precipitates (1–2%) compared to our prior Sc-rich alloy (with four times more Sc) is explained due to the smaller site substitutional energy of Si atoms sitting on the Al sublattice of Al_3Zr versus Al_3Sc.
5. The new alloy exhibits a high threshold stress for creep (17.5–19.3 MPa) and very good creep resistance at 300 °C, behaving as well as a binary Al-0.08Sc at.% alloy, which has a much higher Sc content. The creep resistance increases as the nano-precipitates grow during aging.
6. An apparent activation energy for precipitation of 0.66 ± 0.14 eV was determined in the rapid-growth region (before reaching peak aging). In the coarsening regime, a temporal exponent of −1/3 is obtained, which is consistent with diffusion-limited coarsening.

Acknowledgments

This research was sponsored by the Ford-Northwestern University Alliance. Atom-probe tomography was performed at the Northwestern University Center for Atom-Probe Tomography (NUCAPT). The LEAP tomograph at NUCAPT was purchased and upgraded with funding from NSF-MRI (DMR-0420532) and ONR-DURIP (N00014–0400798, N00014–0610539, N00014-0910781, N00014-1712870) programs. Instrumentation at NUCAPT was supported by the Initiative for Sustainability and Energy at Northwestern University (ISEN). This work made use of the MatCI Facility and the EPIC facility (NUANCE Center) at Northwestern University. NUCAPT, MatCI and NUANCE received support from the MRSEC program (NSF DMR-1720139) through Northwestern's Materials Research Center; NUCAPT and NUANCE also from the Soft and Hybrid Nanotechnology Experimental (SHyNE) Resource (NSF NNCI-1542205). NUANCE received support from the International Institute for Nanotechnology (IIN); the Keck Foundation; and the State of Illinois, through the IIN. DNS and DCD disclose that they have a financial interest in NanoAl LLC which is active in the area of aluminum alloys. The authors kindly thank Drs. J. Boileau and B. Ghaffari (Ford Research Laboratory) for numerous useful discussions.

Appendix A

The strength increment induced by order strengthening ($\Delta\sigma_{ord}$), coherency and modulus mismatch strengthening ($\Delta\sigma_{coh}+\Delta\sigma_{mod}$), and Orowan dislocation looping ($\Delta\sigma_{oro}$) are calculated employing methodologies described in Refs. [51–53]. The expression for order strengthening, $\Delta\sigma_{ord}$, is given by:

$$\Delta\sigma_{ord} = 0.81M\frac{\gamma_{APB}}{2b}\left(\frac{3\pi\varphi}{8}\right)^{1/2} \quad (A1)$$

where M = 3.06 is the mean matrix orientation factor for Al [54], $b = 0.286$ nm is the magnitude of the matrix Burgers vector [55], ϕ is the volume fraction of precipitates, and $\gamma_{APB} = 0.5$ Jm^{-2} is an average value of the Al_3Sc anti-phase boundary (APB) energy for the (111) plane [56–58]. The coherency strengthening $\Delta\sigma_{coh}$ is given by:

$$\Delta\sigma_{coh} = M\alpha_\varepsilon(G\theta)^{3/2}\left(\frac{\langle R\rangle\varphi}{0.5Gb}\right)^{1/2} \quad (A2)$$

where $\alpha_\varepsilon = 2.6$ is a constant [52], G is the shear modulus of Al [55], $\langle R\rangle$ is the mean precipitate radius, and θ is the constrained lattice parameter mismatch at room temperature, calculated using Vegard's rule, and based on precipitate composition as measured by APT (Table 3). Strengthening by modulus mismatch is given by $\Delta\sigma_{mod}$:

$$\Delta\sigma_{mod} = 0.005M(\Delta G)^{3/2}\left(\frac{2\varphi}{Gb^2}\right)^{1/2} b\left(\frac{\langle R\rangle}{b}\right)^{\left(3m/2^{-1}\right)} \quad (A3)$$

where $\Delta G = 42.5$ GPa is the shear modulus mismatch between the matrix and the Al_3Sc precipitates [59], and m is a constant taken to be 0.85 [51]. Finally, strengthening due to Orowan dislocation looping, $\Delta\sigma_{Or}$, is given by Ref. [53]:

$$\Delta\sigma_{Or} = M\frac{0.4}{\pi}\frac{Gb}{\sqrt{1-\nu}}\frac{\ln\left(\frac{2\sqrt{2/3}\langle R\rangle}{b}\right)}{\lambda} \quad (A4)$$

where $\nu = 0.345$ is Poisson's ratio for Al [54]. The edge-to-edge inter-precipitate distance λ, is taken to be the square lattice spacing in parallel planes, which is given by Ref. [60]:

$$\lambda = \left[1.538\varphi^{-1/2} - 1.643\right]\langle R\rangle \quad (A5)$$

References

[1] K.E. Knipling, D.C. Dunand, D.N. Seidman, Criteria for developing castable, creep-resistant aluminum-based alloys – a review, Z. Für Met. 97 (2006) 246–265, https://doi.org/10.3139/146.101249.
[2] E.A. Marquis, D.N. Seidman, Nanoscale structural evolution of Al_3Sc precipitates in Al(Sc) alloys, Acta Mater. 49 (2001) 1909–1919, https://doi.org/10.1016/S1359-6454(01)00116-1.
[3] D.N. Seidman, E.A. Marquis, D.C. Dunand, Precipitation strengthening at ambient and elevated temperatures of heat-treatable Al(Sc) alloys, Acta Mater. 50 (2002) 4021–4035, https://doi.org/10.1016/S1359-6454(02)00201-X.
[4] C.B. Fuller, D.N. Seidman, D.C. Dunand, Mechanical properties of Al(Sc,Zr) alloys at ambient and elevated temperatures, Acta Mater. 51 (2003) 4803–4814, https://doi.org/10.1016/S1359-6454(03)00320-3.
[5] C. Fuller, J. Murray, D. Seidman, Temporal evolution of the nanostructure of Al(Sc,Zr) alloys: Part I – chemical compositions of Al(ScZr) precipitates, Acta Mater. 53 (2005) 5401–5413, https://doi.org/10.1016/j.actamat.2005.08.016.
[6] C. Fuller, D. Seidman, Temporal evolution of the nanostructure of Al(Sc,Zr) alloys: Part II-coarsening of Al(ScZr) precipitates, Acta Mater. 53 (2005) 5415–5428, https://doi.org/10.1016/j.actamat.2005.08.015.
[7] R.A. Karnesky, M.E. van Dalen, D.C. Dunand, D.N. Seidman, Effects of substituting rare-earth elements for scandium in a precipitation-strengthened Al–0.08at. %Sc alloy, Scr. Mater. 55 (2006) 437–440, https://doi.org/10.1016/j.scriptamat.2006.05.021.
[8] R.A. Karnesky, D.N. Seidman, D.C. Dunand, Creep of Al-Sc microalloys with rare-earth element additions, Mater. Sci. Forum 519–521 (2006) 1035–1040 doi:10.4028/www.scientific.net/MSF.519-521.1035.
[9] A. Deschamps, L. Lae, P. Guyot, In situ small-angle scattering study of the precipitation kinetics in an Al–Zr–Sc alloy, Acta Mater. 55 (2007) 2775–2783, https://doi.org/10.1016/j.actamat.2006.12.015.
[10] K.E. Knipling, D.C. Dunand, D.N. Seidman, Nucleation and precipitation strengthening in dilute Al-Ti and Al-Zr alloys, Metallurgical Mater. Trans. A 38 (2007) 2552–2563, https://doi.org/10.1007/s11661-007-9283-6.
[11] K.E. Knipling, D.C. Dunand, D.N. Seidman, Precipitation evolution in Al–Zr and Al–Zr–Ti alloys during isothermal aging at 375–425°C, Acta Mater. 56 (2008) 114–127, https://doi.org/10.1016/j.actamat.2007.09.004.
[12] K.E. Knipling, D.C. Dunand, D.N. Seidman, Precipitation evolution in Al–Zr and Al–Zr–Ti alloys during aging at 450–600°C, Acta Mater. 56 (2008) 1182–1195, https://doi.org/10.1016/j.actamat.2007.11.011.
[13] R.A. Karnesky, D.C. Dunand, D.N. Seidman, Evolution of nanoscale precipitates in Al microalloyed with Sc and Er, Acta Mater. 57 (2009) 4022–4031, https://doi.org/10.1016/j.actamat.2009.04.034.
[14] M.E. van Dalen, T. Gyger, D.C. Dunand, D.N. Seidman, Effects of Yb and Zr microalloying additions on the microstructure and mechanical properties of dilute Al–Sc alloys, Acta Mater. 59 (2011) 7615–7626, https://doi.org/10.1016/j.actamat.2011.09.019.
[15] K.E. Knipling, R.A. Karnesky, C.P. Lee, D.C. Dunand, D.N. Seidman, Precipitation evolution in Al–0.1Sc, Al–0.1Zr and Al–0.1Sc–0.1Zr (at.%) alloys during isochronal aging, Acta Mater. 58 (2010) 5184–5195, https://doi.org/10.1016/j.actamat.2010.05.054.
[16] K.E. Knipling, D.N. Seidman, D.C. Dunand, Ambient- and high-temperature mechanical properties of isochronally aged Al–0.06Sc, Al–0.06Zr and Al–0.06Sc–0.06Zr (at.%) alloys, Acta Mater. 59 (2011) 943–954, https://doi.org/10.1016/j.actamat.2010.10.017.
[17] C. Booth-Morrison, D.C. Dunand, D.N. Seidman, Coarsening resistance at 400°C

of precipitation-strengthened Al–Zr–Sc–Er alloys, Acta Mat. 59 (2011) 7029–7042, https://doi.org/10.1016/j.actamat.2011.07.057.
[18] S.P. Wen, K.Y. Gao, Y. Li, H. Huang, Z.R. Nie, Synergetic effect of Er and Zr on the precipitation hardening of Al–Er–Zr alloy, Scr. Mater. 65 (2011) 592–595, https://doi.org/10.1016/j.scriptamat.2011.06.033.
[19] C. Booth-Morrison, Z. Mao, M. Diaz, D.C. Dunand, C. Wolverton, D.N. Seidman, Role of silicon in accelerating the nucleation of Al_3(Sc,Zr) precipitates in dilute Al–Sc–Zr alloys, Acta. Mat. 60 (2012) 4740–4752, https://doi.org/10.1016/j.actamat.2012.05.036.
[20] C. Booth-Morrison, D.N. Seidman, D.C. Dunand, Effect of Er additions on ambient and high-temperature strength of precipitation-strengthened Al–Zr–Sc–Si alloys, Acta. Mat. 60 (2012) 3643–3654, https://doi.org/10.1016/j.actamat.2012.02.030.
[21] H. Li, J. Bin, J. Liu, Z. Gao, X. Lu, Precipitation evolution and coarsening resistance at 400°C of Al microalloyed with Zr and Er, Scr. Mater. 67 (2012) 73–76, https://doi.org/10.1016/j.scriptamat.2012.03.026.
[22] S.P. Wen, K.Y. Gao, H. Huang, W. Wang, Z.R. Nie, Precipitation evolution in Al–Er–Zr alloys during aging at elevated temperature, J. Alloys Compd. 574 (2013) 92–97, https://doi.org/10.1016/j.jallcom.2013.03.237.
[23] S.P. Wen, K.Y. Gao, H. Huang, W. Wang, Z.R. Nie, Role of Yb and Si on the precipitation hardening and recrystallization of dilute Al–Zr alloys, J. Alloys Compd. 599 (2014) 65–70, https://doi.org/10.1016/j.jallcom.2014.02.065.
[24] Y. Zhang, K. Gao, S. Wen, H. Huang, Z. Nie, D. Zhou, The study on the coarsening process and precipitation strengthening of Al_3Er precipitate in Al–Er binary alloy, J. Alloys Compd. 610 (2014) 27–34, https://doi.org/10.1016/j.jallcom.2014.04.093.
[25] Y. Zhang, J. Gu, Y. Tian, H. Gao, J. Wang, B. Sun, Microstructural evolution and mechanical property of Al–Zr and Al–Zr–Y alloys, Mater. Sci. Eng. A 616 (2014) 132–140, https://doi.org/10.1016/j.msea.2014.08.017.
[26] N.Q. Vo, D.C. Dunand, D.N. Seidman, Improving aging and creep resistance in a dilute Al–Sc alloy by microalloying with Si, Zr and Er, Acta. Mat. 63 (2014) 73–85, https://doi.org/10.1016/j.actamat.2013.10.008.
[27] N.Q. Vo, D.N. Seidman, D.C. Dunand, Aluminum Superalloys for Use in High Temperature Applications, 2015. US20150259773.
[28] E. Çadirli, H. Tecer, M. Şahin, E. Yilmaz, T. Kirindi, M. Gündüz, Effect of heat treatments on the microhardness and tensile strength of Al–0.25wt.% Zr alloy, J. Alloys Compd. 632 (2015) 229–237, https://doi.org/10.1016/j.jallcom.2015.01.193.
[29] N.Q. Vo, D.C. Dunand, D.N. Seidman, Role of silicon in the precipitation kinetics of dilute Al-Sc-Er-Zr alloys, Mater. Sci. Eng. A 677 (2016) 485–495, https://doi.org/10.1016/j.msea.2016.09.065.
[30] A. De Luca, D.C. Dunand, D.N. Seidman, Mechanical properties and optimization of the aging of a dilute Al-Sc-Er-Zr-Si alloy with a high Zr/Sc ratio, Acta Mater. 119 (2016) 35–42, https://doi.org/10.1016/j.actamat.2016.08.018.
[31] Mineralprices.com, (n.d.). http://mineralprices.com/(accessed October 12, 2017).
[32] U.S. Geological Survey, Metal Prices in the United States through 2010: U.S. Geological Survey Scientific Investigations Report 2012–5188, 2013, 204pp.
[33] B.W. Krakauer, J.G. Hu, S.-M. Kuo, R.L. Mallick, A. Seki, D.N. Seidman, J.P. Baker, R.J. Loyd, A system for systematically preparing atom-probe field-ion-microscope specimens for the study of internal interfaces, Rev. Sci. Instrum. 61 (1990) 3390–3398, https://doi.org/10.1063/1.1141590.
[34] B.W. Krakauer, D.N. Seidman, Systematic procedures for atom-probe field-ion microscopy studies of grain boundary segregation, Rev. Sci. Instrum. 63 (1992) 4071–4079, https://doi.org/10.1063/1.1143214.
[35] D.N. Seidman, Three-dimensional atom-probe tomography: advances and applications, Annu. Rev. Mater. Res. 37 (2007) 127–158, https://doi.org/10.1146/annurev.matsci.37.052506.084200.
[36] T.F. Kelly, M.K. Miller, Atom probe tomography, Rev. Sci. Instrum. 78 (2007) 031101, https://doi.org/10.1063/1.2709758.
[37] R.A. Karnesky, Mechanical Properties and Microstructure of Aluminum-scandium with Rare-earth Element or Aluminum Oxide Additions, PhD, Northwestern University, 2007.
[38] R. Lagneborg, B. Bergman, The stress/creep rate behaviour of precipitation-hardened alloys, Metal Sci. 10 (1976) 20–28, https://doi.org/10.1179/030634576790431462.
[39] S. Ochiai, Mechanical Properties of Metallic Composites, Marcel Dekker, New York, 1994.
[40] P. Zhang, S.X. Li, Z.F. Zhang, General relationship between strength and hardness, Mater. Sci. Eng. A 529 (2011) 62–73, https://doi.org/10.1016/j.msea.2011.08.061.
[41] M.E. Krug, A. Werber, D.C. Dunand, D.N. Seidman, Core–shell nanoscale precipitates in Al–0.06 at.% Sc microalloyed with Tb, Ho, Tm or Lu, Acta Mater. 58 (2010) 134–145, https://doi.org/10.1016/j.actamat.2009.08.074.
[42] M.E. Krug, Z. Mao, D.N. Seidman, D.C. Dunand, Comparison between dislocation dynamics model predictions and experiments in precipitation-strengthened Al–Li–Sc alloys, Acta Mater. 79 (2014) 382–395, https://doi.org/10.1016/j.actamat.2014.06.038.
[43] T. Ohashi, R. Ichikawa, Effect of Fe and Si on age hardening properties of supersaturated solid solutions of Al-Zr alloy by rapid solidification, J. Jap. Inst. Met. 34 (1970) 604–610.
[44] S. Hori, T. Kondo, S. Ikeno, Effects of small addition of Si on the precipitation of Al-0.6%Zr alloys, J. Jpn. Inst. Light Metals 28 (1978) 79–84, https://doi.org/10.2464/jilm.28.79.
[45] T. Sato, A. Kamio, G.W. Lorimer, Effects of Si and Ti additions on the nucleation and phase stability of the L12-Type Al3Zr phase in Al-Zr alloys, Mater. Sci. Forum 217–222 (1996) 895–900 doi:10.4028/www.scientific.net/MSF.217-222.895.
[46] H.-H. Jo, S.-I. Fujikawa, Kinetics of precipitation in Al3Sc alloys and low temperature solid solubility of scandium in aluminium studied by electrical resistivity measurements, Mater. Sci. Eng. A 171 (1993) 151–161, https://doi.org/10.1016/0921-5093(93)90401-Y.
[47] A.C. Damask, G.J. Dienes, Point defects in Metals, Gordon and breach, New York, London, 1963. http://hdl.handle.net/2027/mdp.39015039959757.
[48] C.L. Chiang, Statistical Methods of Analysis, World Scientific, River Edge, N.J, 2003.
[49] A. Baldan, Review Progress in Ostwald ripening theories and their applications to nickel-base superalloys Part I: Ostwald ripening theories, J. Mater. Sci. 37 (2002) 2171–2202, https://doi.org/10.1023/A:1015388912729.
[50] K.E. Knipling, Development of a Nanoscale Precipitation-strengthened Creep-resistant Aluminum Alloy Containing Trialuminide Precipitates, Northwestern University, 2006.
[51] A.J. Ardell, Precipitation hardening, MTA 16 (1985) 2131–2165, https://doi.org/10.1007/BF02670416.
[52] A.S. Argon, Strengthening Mechanisms in Crystal Plasticity, Oxford University Press, Oxford, 2007.
[53] A. Kelly, R. Nicholson, Strengthening Methods in Crystals, Elsevier, Amsterdam, 1971.
[54] M.A. Meyers, K.K. Chawla, Mechanical Metallurgy: Principles and Applications, Prentice-Hall, Englewood Cliffs, N.J, 1984.
[55] H.J. Frost, M.F. Ashby, Deformation-mechanism Maps: the Plasticity and Creep of Metals and Ceramics, Pergamon Press, Oxford, 1982.
[56] C.L. Fu, Electronic, elastic, and fracture properties of trialuminide alloys: Al3Sc and Al3Ti, J. Mater. Res. 5 (1990) 971–979, https://doi.org/10.1557/JMR.1990.0971.
[57] E.P. George, D.P. Pope, C.L. Fu, J.H. Schneibel, Deformation and fracture of L12 Trialuminides, ISIJ Int. 31 (1991) 1063–1075, https://doi.org/10.2355/isijinternational.31.1063.
[58] K. Fukunaga, T. Shouji, Y. Miura, Temperature dependence of dislocation structure of $L1_2$–Al_3Sc, Mater. Sci. Eng. A 239–240 (1997) 202–205, https://doi.org/10.1016/S0921-5093(97)00582-0.
[59] R.W. Hyland, R.C. Stiffler, Determination of the elastic constants of polycrystalline Al_3Sc, Scripta Metallurgica Materialia 25 (1991) 473–477, https://doi.org/10.1016/0956-716X(91)90213-K.
[60] E. Nembach, Particle Strengthening of Metals and Alloys, Wiley, New York, 1997.